Preprint Title	Stochastic excitation for high-resolution Atomic Force Acoustic Microscopy imaging: a system theory approach.
Authors	Edgar Cruz-Valeriano, J. J. Gervacio Arciniega, M. A. Hernández Landaverde, Christian I. Enriquez-Flores, Yuri Chipatecua, Aime Gutierrez-Peralta, Rafael Ramírez-Bon, Susana Meraz-Dávila, Joel Moreno Palmerin and J. M. Yañez-Limón
Publication Date	17 Dez 2019
Article Type	Full Research Paper
ORCID® iDs	Edgar Cruz-Valeriano - https://orcid.org/0000-0003-1787-2641

Stochastic excitation for high-resolution Atomic Force Acoustic Microscopy imaging: a system theory approach.

E. Cruz-Valeriano*[3,1], J.J. Gervacio Arciniega[2], M. A. Hernández Landaverde[3], C. I. Enriquez-Flores[4], Y. Chipatecua[3], A. Gutierrez-Peralta[3], R. Ramírez-Bon[3], S. Meraz-Dávila[5,6], Joel Moreno Palmerin[7] and J. M. Yañez-Limón[3]

Address: [1]Universidad Cuauhtémoc. Blvd. Bernardo Quintana A. #229. Fracc. Los Arcos C.P. 76060, Querétaro, Querétaro, México.; [2]CONACYT-Facultad de Ciencias Físico-Matemáticas, Benemérita Universidad Autónoma de Puebla, Av. San Claudio y Av. 18 sur, Col. San Manuel Ciudad Universitaria, C.P. 72570, Puebla, Puebla, México.; [3]CINVESTAV. Libramiento Norponiente #2000 C.P. 76230, Fracc. Real de Juriquilla, Querétaro, Querétaro, México.; [4]Facultad de Ciencias Físico Matemático, Universidad Autónoma del Estado Chiapas, Carr. Emiliano Zapata Km 8 Tuxtla Gutiérrez, Chiapas C.P. 29050, México.; [5]Centro de Investigación Científica y de Educación Superior de Ensenada, Baja California. Carretera Ensenada - Tijuana No. 3918, Zona Playitas, CP. 22860, Ensenada, B.C. México.; [6]Centro de Nanociencias y Nanotecnología, UNAM, Km 107 Carretera Tijuana-Ensenada C.P. 22800. Ensenada, Baja California, México. and [7]Departamento de Minas, Metalurgía y Geología, Universidad de Guanajuato. Ex Hacienda San Matías s/n C.P. 36020. Guanajuato, Guanajuato, México.

Email: E. Cruz-Valeriano - edcruz@ucq.edu.mx

* Corresponding author

Abstract

In this work, a high-resolution Atomic Force Acoustic Microscopy imaging technique is shown in order to obtain the local indentation modulus at nanoscale using a model which gives a quantitative relationship between a set of contact resonance frequencies and indentation modulus through a white-noise excitation. This technique is based on white-noise excitation for system identification due to non-linearities in the tip-sample interaction. During a conventional scanning, a Fast Fourier Transform is applied to the deflection signal which comes from the photo-diodes of the Atomic Force Microscopy (AFM) for each pixel, while the tip-sample interaction is excited by a white-noise signal. This approach allows the measurement of several vibrational modes in a single step with high frequency resolution, less computational data and at a faster speed than other similar techniques. This technique is referred to as Stochastic Atomic Force Acoustic Microscopy (S-AFAM), where the frequency shifts with respect to free resonance frequencies for an AFM cantilever can be used to determine the mechanical properties of a material. S-AFAM is implemented and compared to a conventional technique (Resonance Tracking-Atomic Force Microscopy, RT-AFAM), where a graphite film over a glass substrate sample is analyzed. S-AFAM can be implemented in any AFM system due to its reduced instrumentation compared to conventional techniques.

Keywords

Atomic Force Microscopy; Fast Fourier Transform; Mechanical properties; System theory; White noise

Introduction

There are many methods to measure mechanical properties at nanoscale, some of them are based on either indentation or any other physical phenomena [1,2]. However, each method has its own limits due to instrumentation capabilities, contact geometries and so forth. Additionally, some of these methods can be destructive or can provide insufficient resolution as dimensions shrink further[1].

Atomic Force Microscopy (AFM) has demonstrated to be a fundamental tool in nanotechnology science [3] since this offers a non-destructive alternative for measuring mechanical properties at nanoscale using the small size of the cantilever tip (radius$\sim$5-50nm).

Conventional AFM methods for mechanical properties measurement are based either on force-displacement curves or resonance frequencies [1]. Force-displacement works better when the stiffness of the cantilever is comparable to that of the test material. This is suitable for soft materials loosing effectiveness as the material stiffness increases. On the other hand, the contact resonance method is ideal when the material stiffness is greater, where the cantilever vibration at or near its resonant frequencies is used. This is suitable for stiff materials such as ceramics or metals [1,4]. The functionality can be found in the resonant vibrational modes of the cantilever when it is excited either by an external actuator or by an actuator attached to the AFM cantilever holder [1]. When the tip is out of contact with the sample, the resonance modes occur at a specific frequency that depends on the geometrical and material properties of the cantilever, on the other hand, when the tip is placed in contact, the resonance modes increase the frequencies due to tip-sample interaction. In this manner, the mechanical properties of the sample can be deduced from these frequency shifts and a suitable model [1,4-10].

The methods which use the resonance frequencies are often labeled as acoustic or ultrasonic methods due to frequency of the vibration involved ($\sim$100kHz-3MHz) [1,8,11]. Among them are: ultrasonic force microscopy (UFM) [12], heterodyne force microscopy [13], ultrasonic atomic force microscopy (UAFM), atomic force acoustic microscopy (AFAM) [1], bimodal AFM [14], resonance tracking-Atomic Force Microscopy (RT-AFAM) [6], band excitation [9], dual-frequency resonance-tracking atomic force microscopy [15], nanomechanical holography [2], G-mode [16], triple frequency atomic force microscopy[17] and so on. Even though these methods offer realiable measurements, these can only measure one or three resonant vibrational modes with a relative frequency resolution, and in some cases the involved instrumentation can be very complex [2,9,15,16,18] making the system excitation restricted to purely sinusoidal signals and to the lock-in time constant, which reduces the time response of the overall measurement when a lock-in amplifier is used [9,16,19].

In this work, an AFM technique based on resonance frequency shifts is shown where the main advantages of this technique are: requires a reduced instrumentation, offers higher frequency resolution at different resonant vibrational modes, obtains more than one vibrational mode in a single step and gives indentation modulus mappings. These tasks are possible when *system theory* [20] is taken into account, specifically the *identification system problem* [21]. Here, a mathematical model, which describes the free/contact cantilever resonance frequencies, is obtained when the tip-sample interaction is perturbed by a stochastic signal. For this reason, the technique is referred to as Stochastic-Atomic Force Acoustic Microscopy (S-AFAM).

S-AFAM works as follows: While the commercial AFM is scanning on contact mode conventionally, the tip-sample interaction is excited by a white-noise signal generated by a function waveform generator equipment through a piezoelectrical actuator below the tip-sample. At the same time, a Fast Fourier Transform (FFT) is computed to the deflection signal from photo-diodes by data acquisition equipment for each pixel of the sample, where each FFT spectrum is stored in a hard-disk. This way of measurement does not use a lock-in amplifier which reduces the time response of the overall measurement and enhances the frequency window for analysis. At the end of the scanning, all the acquired FFT spectra make a 128×128-pixel mapping, where the detection of frequency shifts is recorded with a resolution of 153.8 Hz. Then, an off-line process is carried out using a program routine on Matlab™which is based on a mathematical model that relates the contact resonance frequencies with an indentation modulus value when a white-noise excitation is taken into account. This model is based on the Power Spectral Density (PSD), Harmonic Oscillator Model. At the end of the process, an indentation modulus mapping is obtained through this methodology.

This paper is organized as follows. First of all, the prototype is described with further details including the acquisition data process in the *Materials and methods section*. In the next section, the mathematical background is described in *Experimental details* where the Power Spectral Density is described for a free cantilever and a contact cantilever, both cases excited by white-noise signal. In the *Results and discussion section* the obtained images using S-AFAM are shown, explained within further detail and compared to RT-AFAM. Finally, we end with some conclusions about the capabilities of the proposed technique.

Materials and methods

S-AFAM takes an optimal instrumentation, which is plugged in to a commercial AFM equipment, see Figure 1. The instrumentation consists of:

- A SPM, Bruker / Veeco / Digital Instruments Nanoscope IV Dimension 3100 equipment is used, this was upgraded with a closed-loop x-y nanopositioning stage (nPoint, Inc. NPXY100), a signal access module (SAM) accessory which was used for signal input/output to the AFM, and supported on a floating air table and equipped with an acoustical isolation chamber which minimizes the external thermal and vibrational disturbances, respectively.
- Data acquisition and FFT processing were carried out using NI PXIe-1073 equipment, which includes a NI 7961R FPGA, NI 5762 digitizer at 200MS/s/ch, and PXI 6363DAQ from National Instruments™.
- White-noise signal is generated by a function waveform generator HP/Agilent 33120A.
- BudgetSensors™diamond-coated silicon probes, 450 μm long with a 0.2 Nm^{-1} spring constant were used.
- All experiments were carried out in dry air at a temperature of 21.0±0.1°C and humidity of $2\% \pm 1\ \%$.

It is very important to define the appropiate signal in order to make the entire system perturbed, this allows to have enough information about the system dynamics. For this work, a stochastic signal is used for the tip-sample excitation because it can extract all the system dynamics, i.e. *persistent excitation* in the system theory field [22,23].

The proposed technique works when a FFT is computed by NI PXIe-1073 equipment taking into account the deflection signal from photo-diodes for a specific point from the sample to be measured during a conventional scanning of 128×128-pixel in an AFM. Here, while a system is executing this task, HP/Agilent 33120A is exciting the tip-sample through an external piezoelectric actuator below the sample using a white-noise signal. White-noise approximation is used for this pur-

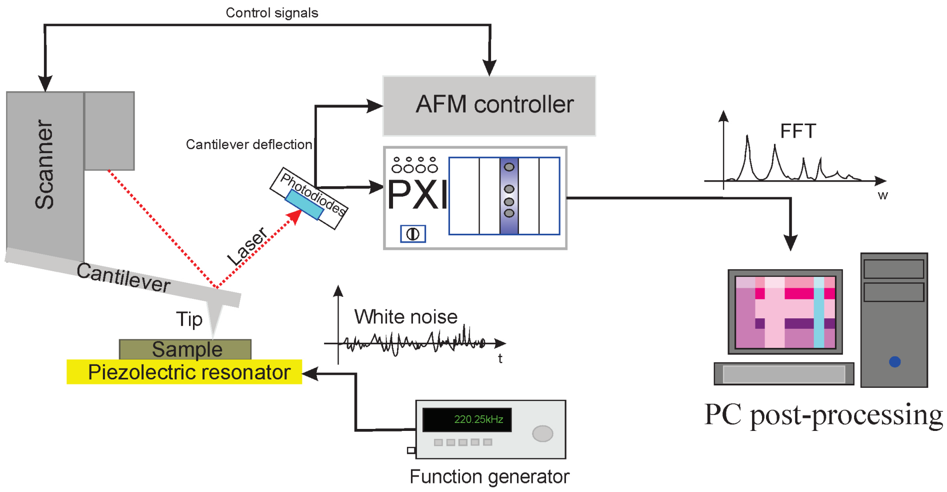

Figure 1: Experimental setup for S-AFAM, using a NI PXIe-1073 equipment and a function waveform generator HP/Agilent 33120A.

pose because it can excite the tip-sample system using a 10MHz flat-bandwidth signal generated by HP/Agilent 33120A equipment [20-24].

Once the FFT spectra have been obtained in a 128×128-pixel mapping, it is saved in a hard-disk for off-line processing. Each pixel has a FFT spectrum, where they each have at least four resonance frequencies, see Figure 2. An off-line processing is computed for each resonance frequency taking into account a simple Harmonic Oscillator Model fitting. Finally, the FFT spectra mapping is transformed into an indentation modulus mapping using a mathematical model based on the reduced elasticity modulus and PSD model, where the latter is used due to it is the ideal tool for stochastic process in frequency domain[25].

This way of enhancement allows the measurement of several resonance frequencies where other conventional techniques do not in one single step and without a lock-in amplifier. To show the capabilities of this technique, a graphite film was deposited on a glass substrate using a sputtering technique, which was characterized by the conventional method RT-AFAM [6] and by the proposed technique, S-AFAM.

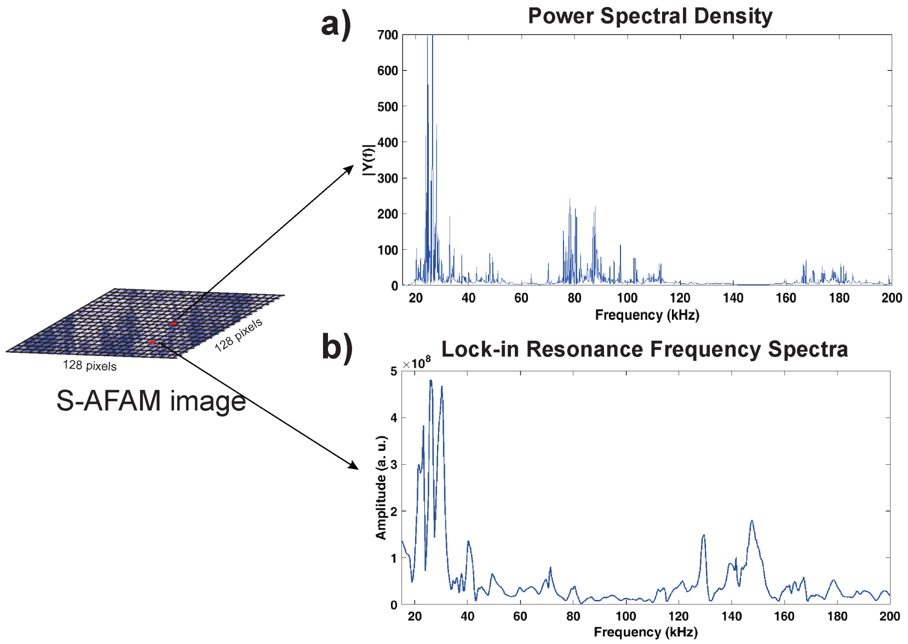

Figure 2: Contact resonance frequencies for a graphite film over glass corning. a) Resonance flexural modes acquired using S-AFAM, b) Resonance flexural modes acquired using a lock-in.

Experimental details

Dynamic model

It is important to have a mathematical model in order to determine that the tip-sample interaction excited by white-noise can extract the resonance frecuencies for a free/contact cantilever. For this objective, the model by Vazquez et al. [26-28] was taken into account, and then used into a PSD model to make a transformation from resonance frequency to indentation modulus. This kind of model is necessary since the white-noise signal belongs to the power signals set. In other words, these signals offer infinite energy[24,25].

For this work, the tip-sample interaction must be studied as a system[20,22], see Figure 3. The input of the system is considered as the excitation signal through a piezoelectrical actuator, which can be controlled in amplitude and frequency domain, and the output of the system is considered as the deflection signal from the photo-diodes of the AFM.

In this manner, the classical Euler-Bernoulli beam equation is used, which is expressed by Vazquez

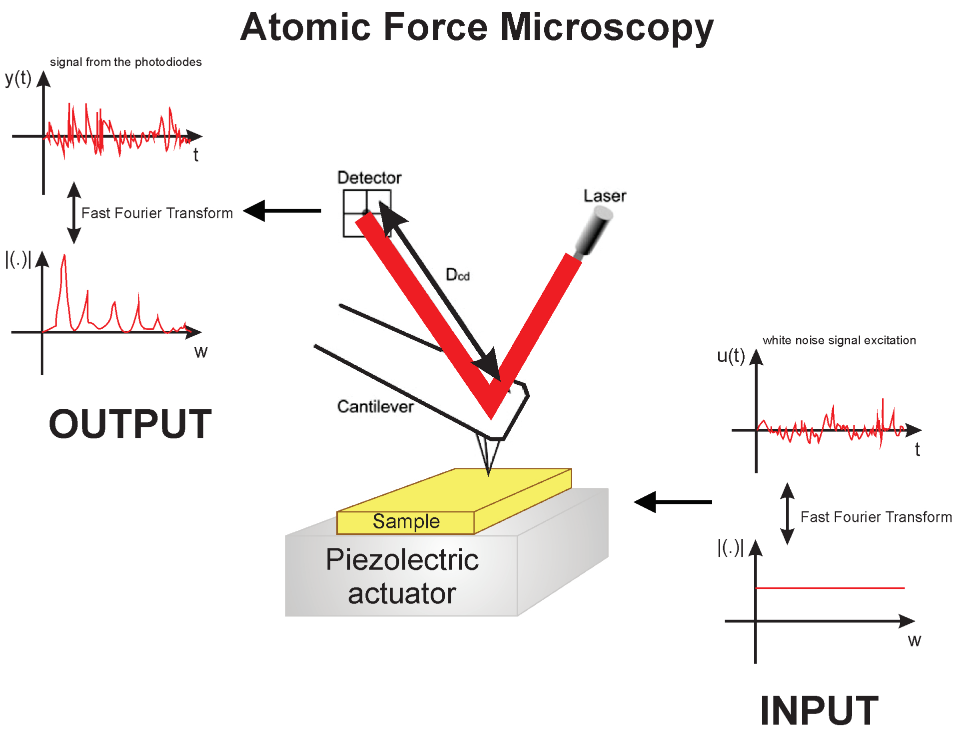

Figure 3: AFM system, piezoelectrical signal excitation is considered as the input, while the deflection signal from the photo-diodes is considered as the output.

et al. as [26-28]

$$EI\frac{\partial^4 z(x,t)}{\partial x^4} + c\frac{\partial z(x,t)}{\partial t} + m\frac{\partial^2 z(x,t)}{\partial t^2} = -u(t), \tag{1}$$

where EI is the flexural stiffness, c corresponds to the damping due to viscous friction, m to the mass per unit length and $z(x,t)$ is the deflection of the cantilever defined for a displacement toward the sample, t is time, $x \in [0, L]$, $u(t)$ is a uniform force per unit length acting along the cantilever and L is the length of the cantilever, respectively. The boundary conditions at the fixed end are

$$\begin{aligned} z(x,t)\Big|_{x=0} &= 0, \\ \frac{\partial z(x,t)}{\partial x}\Big|_{x=0} &= 0, \end{aligned} \tag{2}$$

and at the tip end are

$$\left.\frac{\partial^2 z(x,t)}{\partial x^2}\right|_{x=L} = 0,$$

$$EI\left.\frac{\partial^3 z(x,t)}{\partial x^3}\right|_{x=L} + f(t) = -q(t), \tag{3}$$

where $q(t)$ is the input force acting perpendicular to the cantilever and $f(t)$ is the interaction force between the cantilever and the surface expressed by Derjaguin-Muller-Toporov (DMT) model [1] as

$$f(t) = -\frac{HR}{6a_0^2} + \frac{4}{3}E^*\sqrt{R}(z_s - z(x,t) + a_0)^{3/2}, \tag{4}$$

where H is Hamaker constant, R is the tip radius, E^* is the reduced elastic modulus between the tip and the sample, a_0 is the interatomic distance and z_s is considered as the distance from the sample to the tip of the undeflected cantilever, which is described by the force $f(t)$ linearized around a z_0 point as

$$f(t) = -\left.\frac{\partial f(t)}{\partial z(L,t)}\right|_{z_0} = -2E^*\sqrt{R(z_s - z_0 + a_0)}, \tag{5}$$

in this equation $k_{ts} = -(\partial f(t)/\partial z(L,t))|_{z_0}$ represents the contact stiffness. Then, the linearized model around z_0 according to Equation 3 is

$$EI\left(\left.\frac{\partial^3 z(x,t)}{\partial x^3}\right|_{x=L} - \frac{\widehat{k}_{ts}}{3L^3}z(x,t)\right) = -q(t), \tag{6}$$

where

$$k_{ts} = \frac{3EI}{L^3}\hat{k}_{ts}. \tag{7}$$

Using the boundary conditions, the Laplace transform is applied to Equation 1, the cantilever deflection is described by

$$
\begin{aligned}
Z(x,s) \;=\; & cosh(\lambda(s)x)\left[A_1 cos(\lambda(s)x) + A_2 sin(\lambda(s)x)\right] + \\
& sinh(\lambda(s)x)\left[A_3 cos(\lambda(s)x) + A_4 sin(\lambda(s)x)\right] + \\
& \frac{U(s)}{4EI\lambda(s)^4}, \qquad (8)
\end{aligned}
$$

where

$$\lambda(s) = \sqrt[4]{\frac{cs + ms^2}{4EI}}, \qquad (9)$$

and the constants A_1, A_2, A_3 and A_4 can be found using boundary conditions.

Free cantilever transfer function

For the free cantilever response excited by white-noise, Equation 8 has to be considered as a transfer function for a PSD treatment. This transfer function describes the relationship between the piezoelectric actuator excitation and the free cantilever deflection according to the system described in Figure 3, this is expressed using some equalities [29] as follows

$$\frac{Z_{free}(x,s)}{U(s)} = \frac{-4L^3 \prod_{n=1}^{\infty}\left[1 - \frac{\lambda^4 L^4}{n_n^4}\right]}{24EI \prod_{n=1}^{\infty}\left[1 + \frac{\lambda^4 L^4}{d_n^4}\right]}, \qquad (10)$$

where n_n and d_n are the n-th roots of

$$
\begin{aligned}
tan(n_n) = tanh(n_n) \mid n_n > 0, \\
cos(d_n)cosh(d_n) = -1 \mid d_n > 0,
\end{aligned}
$$

respectively.

Thus, Equation 10 is expanded using Equation 9 as

$$\frac{Z(x,s)}{U(s)} = \left(\frac{-4L^3}{3EI}\right)\left[\frac{\prod_{n=1}^{\infty}\left(\frac{-mL^4}{4n_n^4}s^2 - \frac{c}{4n_n^4}s + \frac{EI}{L^4}\right)}{\prod_{n=1}^{\infty}\left(\frac{m}{d_n^4}s^2 + \frac{c}{d_n^4}s + \frac{EI}{L^4}\right)}\right], \tag{11}$$

Now, PSD has to be computed from Equation 11 since the system is excited by a stochastic signal [24,25]. For this work, the signal excitation to be considered is white-noise signal because it features an infinite flat-bandwidth. White-noise is defined as a scalar second-order discrete-time stochastic process for voltage generated by the function waveform generator, $V_{(-\infty,\infty)}$, and its properties are

$$\eta(k) = E\{V_k\} = 0, \text{ for all } k, -\infty < k < \infty,$$

$$R(k,k+l) = E\{V_k V_{k+l}\} = r\delta(k) \text{ for all } -\infty < k, l < \infty.$$

where $r \geq 0$, mean $E\{V_k\}$ is the expected value of the random variable $V(k)$, the autocorrelation $E\{V_k V_{k+l}\}$ is the expected value of the product $V_k V_{k+l}$, and $\delta(k)$ is Dirac delta function [24,25,30]. Then, a PSD must be calculated for each pole and zero. The PSD for a pole is calculated taking into account a n-th pole from Equation 11 as

$$G_{Pn-free}(s) = \frac{\frac{d_n^4}{m}}{s^2 + \frac{c}{m}s + \frac{EId_n^4}{mL^4}},$$

which can be transformed into matrix form [20] for sake clarity as

$$\begin{aligned}
\begin{bmatrix} \dot{x_1} \\ \dot{x_2} \end{bmatrix} &= \begin{bmatrix} 0 & 1 \\ -\frac{EId_n^4}{mL^4} & -\frac{c}{m} \end{bmatrix}\begin{bmatrix} x_1 \\ x_2 \end{bmatrix} + \begin{bmatrix} 0 \\ 1 \end{bmatrix} q, \\
y_1 &= \begin{bmatrix} \frac{d_n^4}{m} & 0 \end{bmatrix}\begin{bmatrix} x_1 \\ x_2 \end{bmatrix} + [0]q, \qquad (12)
\end{aligned}$$

where $\dot{x_1}$ is the cantilever deflection, $\dot{x_2}$ is the derivative for cantilever deflection and q is the same input force described in Equation 3.

The PSD model [24] for a second order system is

$$G_{yy}(\omega) = C(-j\omega I - A)^{-1} B G_{\omega\omega}(\omega) B^T (j\omega I - A)^{-T} C^T, \tag{13}$$

where ω is the frequency,

$$A = \begin{bmatrix} 0 & 1 \\ -\frac{EId_n^4}{mL^4} & -\frac{c}{m} \end{bmatrix}, B = \begin{bmatrix} 0 \\ 1 \end{bmatrix}, C = \begin{bmatrix} \frac{d_n^4}{m} & 0 \end{bmatrix}, \tag{14}$$

$\bar{\lambda} = -j\omega$ as the complex conjugate of λ, the white-noise power is

$$E\left[\omega(t)\omega(\tau)\right] = V\delta(t-\tau),\, BG_{\omega\omega}(\omega)B^T = \begin{bmatrix} 0 & 0 \\ 0 & V \end{bmatrix}, \tag{15}$$

and V is the voltage amplitude for white-noise signal produced by the function waveform generator.

Thus, the Equation 13 for n-th pole becomes

$$G_{Pyy-free}(\omega) = \frac{\frac{Qd_n^8}{m^2}}{\left(\omega^2 - \frac{EId_n^4}{mL^4}\right)^2 + \frac{c^2}{m^2}\omega^2}. \tag{16}$$

Now, the PSD for a n-th zero is calculated taking into account Equation 11 as

$$G_{Zn-free}(s) = \frac{\frac{-m}{4n_n^4}}{s^2 - \frac{c}{m}s - \frac{4EIn_n^4}{mL^4}},$$

which can be transformed into matrix form for sake clarity as

$$\begin{aligned}
\begin{bmatrix} \dot{x_2} \\ \dot{x_3} \end{bmatrix} &= \begin{bmatrix} 0 & 1 \\ \frac{4EIn_n^4}{mL^4} & -\frac{c}{m} \end{bmatrix} \begin{bmatrix} x_3 \\ x_4 \end{bmatrix} + \begin{bmatrix} 0 \\ 1 \end{bmatrix} q, \\
y_2 &= \begin{bmatrix} \frac{-m}{4n_n^4} & 0 \end{bmatrix} \begin{bmatrix} x_3 \\ x_4 \end{bmatrix} + [0]q,
\end{aligned} \tag{17}$$

where $\dot{x_3}$ is white-noise, $\dot{x_4}$ is the derivative for white-noise.

Using the same formula described in Equation 13 for PSD, and the next equalities

$$A^{'} = \begin{bmatrix} 0 & 1 \\ \frac{4EIn_n^4}{mL^4} & -\frac{c}{m} \end{bmatrix}, B^{'} = \begin{bmatrix} 0 \\ 1 \end{bmatrix}, C^{'} = \begin{bmatrix} \frac{-m}{4n_n^4} & 0 \end{bmatrix}, \tag{18}$$

$\bar{\lambda} = -j\omega$ as the complex conjugate of λ, and the white-noise power described in Equation 15. The PSD for a n-th zero becomes

$$G_{Zyy-free}(\omega) = \frac{\frac{Qm^2}{16n_n^8}}{\left(\omega^2 + \frac{4EIn_n^4}{mL^4}\right)^2 + \frac{c^2}{m^2}\omega^2}. \tag{19}$$

Finally, taking into account Equation 16 and Equation 19, the PSD for Equation 10 when it is excited by white-noise is

$$G_{free}(\omega) = \frac{-4L^3}{3EI} \frac{\prod_{n=1}^{\infty} \left[\frac{\left(\omega^2 + \frac{4EIn_n^4}{mL^4}\right)^2 + \frac{c^2}{m^2}\omega^2}{\frac{Qm^2}{16n_n^8}} \right]}{\prod_{n=1}^{\infty} \left[\frac{\frac{Qd_n^8}{m^2}}{\left(\omega^2 - \frac{EId_n^4}{mL^4}\right)^2 + \frac{c^2}{m^2}\omega^2} \right]}, \tag{20}$$

this Equation could possibly be obtained since the model was linearized. For this reason, the PSD can be calculated for each pole and zero independently in the frequency domain [20,25,31], and then used altogether for the free cantilever transfer function , Equation 11.

Contact cantilever transfer function

The transfer function for a contact cantilever is defined from Equation 8 as

$$\frac{Z_{cont}(x,s)}{U(s)} = \frac{\frac{8L^3}{3}\prod_{n=1}^{\infty}\left[1+\frac{4\lambda^4L^4}{n_n^4}\right]}{8EI(1+\hat{k}_{ts})\prod_{n=1}^{\infty}\left[1+\frac{4\lambda^4L^4}{d_n^4}\right]}, \tag{21}$$

where $\hat{k}_{ts} > -1$, n_n and d_n are the nth-roots of

$$tan(n_n) = tanh(n_n) \mid n_n > 0,$$

$$\frac{3\hat{k}_{ts}}{d_n^3}\left[sinh(d_n)cos(d_n) - cosh(d_n)sin(d_n\right] = 1 + cos(d_n)cosh(d_n) \mid d_n > 0,$$

respectively.

And now, using the same methodology as the last section to obtain the transfer function for a free cantilever excited by white-noise, the PSD for a contact cantilever is carried out. From Equation 21 the n-th pole is described by

$$G_{Pn-cont}(s) = 8EI(1+\hat{k}_{ts})\left[1+\frac{4\lambda^4L^4}{d_n^4}\right], \tag{22}$$

using Equation 13, the PSD for a n-th pole is calculated as

$$G_{Pyy-cont}(w) = \frac{\frac{Qd_n^8}{64(1+\hat{k}_{ts})^2L^8m^2}}{\left(\omega^2 - \frac{EId_n^4}{mL^4}\right)^2 + \frac{c^2}{m^2}\omega^2}, \tag{23}$$

and also from Equation 21 the n-th zero is described by

$$G_{Zn-cont} = \frac{8L^3}{3}\left[1+\frac{4\lambda^4L^4}{n_n^4}\right], \tag{24}$$

using Equation 13, the PSD for a n-th zero is calculated as

$$G_{Zyy-cont}(w) = \frac{\left(\omega^2 - \frac{EIn_n^4}{mL^4}\right)^2 + \frac{c^2}{m^2}\omega^2}{\frac{9QE^2I^2n_n^8}{m^2L^8}}. \tag{25}$$

Finally, using Equation 23 and Equation 25, the PSD for contact cantilever is calculated for Equation 21 as

$$G_{cont}(\omega) = \frac{\prod_{n=1}^{\infty}\left[\frac{\left(\omega^2 - \frac{EIn_n^4}{mL^4}\right)^2 + \frac{c^2}{m^2}\omega^2}{\frac{9QE^2I^2n_n^8}{m^2L^8}}\right]}{\prod_{n=1}^{\infty}\left[\frac{\frac{Qd_n^8}{64(1+\hat{k}_{ts})^2L^8m^2}}{\left(\omega^2 - \frac{EId_n^4}{mL^4}\right)^2 + \frac{c^2}{m^2}\omega^2}\right]}. \tag{26}$$

Results and Discussion

Other similar works in literature give an indentation modulus for each resonance frequency making a sample to have more than one value for indentation modulus. In this work, Equation 20 and Equation 26 are useful because it gives a quantitative relationship between a set of resonance frequencies and a unique indentation modulus through a white-noise excitation. To see the validation of this model, some simulations and measurements are presented.

Equation 20 and Equation 26 are simulated with the following numerical data extracted from [27]: $E = 169.7$GPa, $I = 3.64 \times 10^{-22}$m^4, $c = 1 \times 10^{-18}$kg/ms and $m = 4.08 \times 10^{-7}$kg/m. For the free cantilever case, the simulation is shown in Figure 4(a). In this figure, a difference in resonance frequencies can be seen between a cantilever with $L = 300\mu$m and another one with $L = 500\mu$m, i.e. when the cantilever is shorter, the resonance frequencies increase. Using these computed free resonance frequencies, the geometry for a real cantilever can be known if a suitable program routine is used to search for the best cantilever fitted to these frequencies.

For the contact cantilever case, the simulation is shown for three cantilevers with a contact stiffness of 10N/m: $L = 300\mu$m, $L = 400\mu$m and $L = 500\mu$m, see Figure 4(b). The behavior for resonance frequencies is similar to free cantilever, i.e. when the cantilever is shorter, the resonance frequencies increase. This result indicates that the length of the cantilever must be taken into account for the sensitivity, where the range of frequencies depends on the local mechanical properties of the sample.

When a contact cantilever with $L = 400\mu$m is taken into account and only its contact stiffness is changed, it can be seen how the resonance frequencies increase as the contact stiffness does too. Three simulations are shown for contact stiffness $\hat{k}_{ts}$: 1N/m, 10N/m and 100N/m, see Figure 4(c). These simulations show that it is possible to have a quantitative relationship between a set of resonance frequencies and an indentation modulus value.

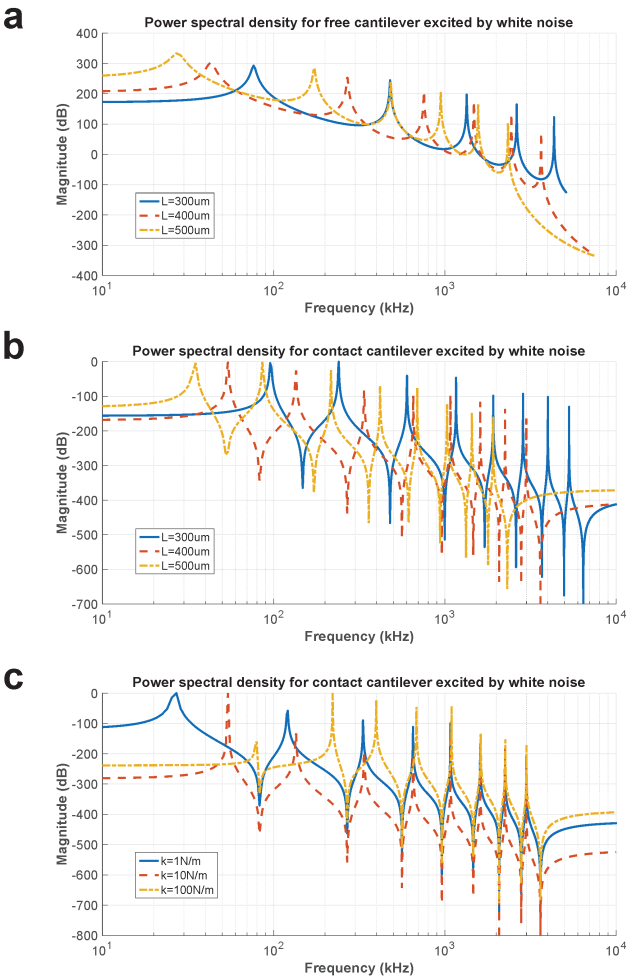

Figure 4: PSD simulation. a) Free cantilever:$L = 300\mu$m(blue line), $L = 400\mu$m(dashed red line) and $L = 500\mu$m(dotted yellow line), b) Contact cantilever: $L = 300\mu$m(blue line), $L = 400\mu$m(dashed red line) and $L = 500\mu$m(dotted yellow line), c) Contact cantilever for $L = 400\mu$m: $\hat{k}_{ts} = 1$N/m(blue line), $\hat{k}_{ts} = 10$N/m(dashed red line), $\hat{k}_{ts} = 100$N/m(dotted yellow line).

Now, the simulated results bring the enough support for an experiment in order to show the capabilities of this technique. First, the geometrical parameters for the experimental cantilever must be known since the resonance frequency transformation into indentation modulus requires these values. For this purpose, a resonance frequency spectrum was acquired for free cantilever using white-noise as excitation signal and the FFT algorithm. These resonance frequencies were fitted according to a database which was computed using the free cantilever model described in Equation 20, and *particle swarm optimization algorithm*[32-35] in order to obtain the geometrical parameters for the experimental cantilever. The database describes each cantilever according to: length L, width a, thickness b, inertia moment $I = ab^3/12$, linear mass $m = \rho A$, where A is the cross-section area of the cantilever and $\rho = 2330\text{kg}/m^3$ [36] is the density of the cantilever. The database has 10000 cantilevers where $L \in [440, 500]\,\mu$m, $a \in [40, 50]\,\mu$m, $b \in [1, 3]\,\mu$m.

The optimization criteria is

$$J = e_{rms} = \sqrt{\frac{1}{N}\sum_{n=1}^{N}\left(f_n - \hat{f}_n\right)^2}, \tag{27}$$

where e_{rms} is root mean square error, f_n is the n-th measured free resonance frequency, and $\hat{f}_n$ is the n-th theoretical free resonance frequency. For this work, using this optimization algorithm, the best cantilever results with the following dimensions: $L = 460\mu$m, $a = 58\mu$m, $b = 1.8\mu$m.

The free resonance frequencies for the fitted experimental cantilever are compared with the experimental ones and with those obtained by using Finite Element Process (FEA) [36], see Table 1. There is an average error of 3.496$\%$ between the experimental frequencies and those obtained by using the proposed model, meanwhile there is a higher average error of approximately 5.652$\%$ between the experimental frequencies and those obtained by using FEA. Although, there is an almost homogeneous error of 4$\%$ using the proposed model, it can provide a good approximation about the cantilever geometry using white-noise as an excitation signal. This result reinforces S-AFAM as a technique for the measurement of mechanical properties.

Also, the k_{lever} was calculated and compared with the fitted experimental cantilever used in this

Table 1: Modeled versus observed dynamic behavior for an AFM free cantilever.

Mode	**Experiment (kHz)**	**FEA (kHz)**	**Error (%)**	**Model (kHz)**	**Error (%)**
1	70.102	58.274	16.872	73.490	4.832
2	204.530	198.220	3.085	205.800	0.620
3	386.384	383.350	0.785	403.300	4.378
4	639.992	651.950	1.868	666.600	4.157

experiment, the comparison can be seen in Table 2. The first value was obtained from the manufacturer data, while the second value was obtained using the method by Sader[19], and the third value was obtained using $k_{lever} = \frac{3EI}{L^3}$, where the geometrical values were taken from the fitting process. It is important to notice that there is a good agreement between the Sader method and the proposed model which makes S-AFAM a reliable method.

Table 2: Modeled versus other methods for k_{lever}.

Manufacturer $\mathbf{k}_{lever}$ (N/m)	**Sader method $\mathbf{k}_{lever}$ (N/m)**	**Model $\mathbf{k}_{lever}$ (N/m)**
0.2	0.179±6.91%	0.1474±3.49%

Then, a conventional AFM mapping for a graphite film over a glass substrate was carried out using a white-noise signal as excitation for tip-sample interaction. During this task, each pixel has a FFT computed and stored in a hard-disk. The Figure 4(c) shows that the contact stiffness can be obtained from these contact resonance frequencies, where it is important to notice that a set of resonance frequencies can provide an unique value for contact stiffness according to Equation 26. For this purpose, a mapping transformation from resonance frequencies to contact stiffness was obtained using a database for 8000 values for contact stiffness from 0.5N/m to 4000N/m with a step of 0.5N/m using the geometrical values for the cantilever obtained from the fitting process, see Figure 5.

A conventional AFM topography image is shown in Figure 6(a) where each material is indicated by a label, the graphite film was made using sputtering technique with $7nm$ of thickness. Even though

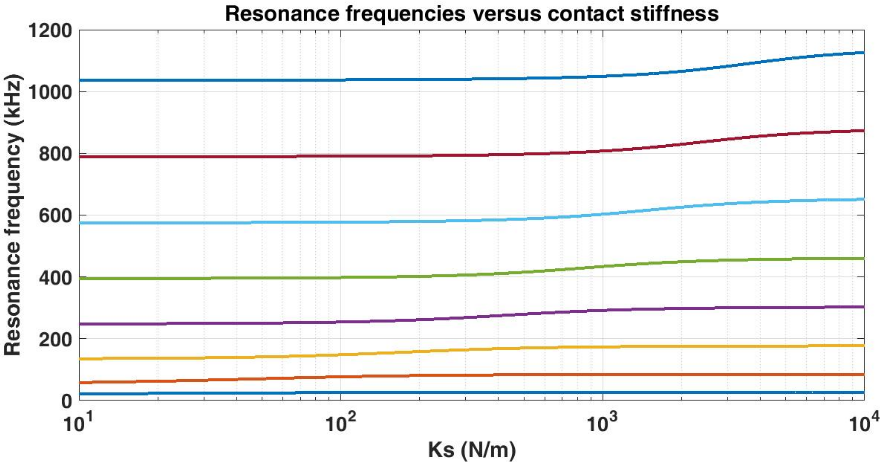

Figure 5: Contact stiffness versus flexural resonance frequencies using a cantilever with geometrical parameters: $L = 460\mu$m, $a = 58\mu$m, $b = 1.8\mu$m.

the sample has two materials, it is very to difficult to see a difference using conventional AFM measurement. For this reason, a conventional AFM technique based on contact resonance was used, in this case RT-AFAM [6], where the sample must show two resonance zones: one for glass and the other one for graphite, respectively. Figure 6(b) shows a RT-AFAM image where the two materials can be appreciated, but the difference between the materials is not enough.

Now, S-AFAM was used to obtain images with higher resolution frequency, making the difference between graphite and glass visible, see Figure 6(c), (d), (e) and (f). When the frequency window goes higher, not only an a higher difference is appreciated between two materials, but some details can also be seen, which are attributed to the aggregates and imperfections of the deposition technique between the glass substrate and the same material deposited on it. In Figure 6(d), one kind of these details is appreciated in the left-bottom zone where the resonance frequency contribution is higher for glass than graphite, which could be explained if the contact deposition was deposited with some imperfections. The maximum difference between two materials is shown in Figure 6(d) and (e) where the resonance frequency peaks are greater than in any other image. It is important to notice that Figures 6(c), (d), (e) and (f) were acquired during approximately 3 hours using S-AFAM, while the same result using RT-AFAM would have taken more than 8 hours with lower resolution as seen in Figure 6(b).

Finally, it is well known that the tip-sample interaction provides information about the contact

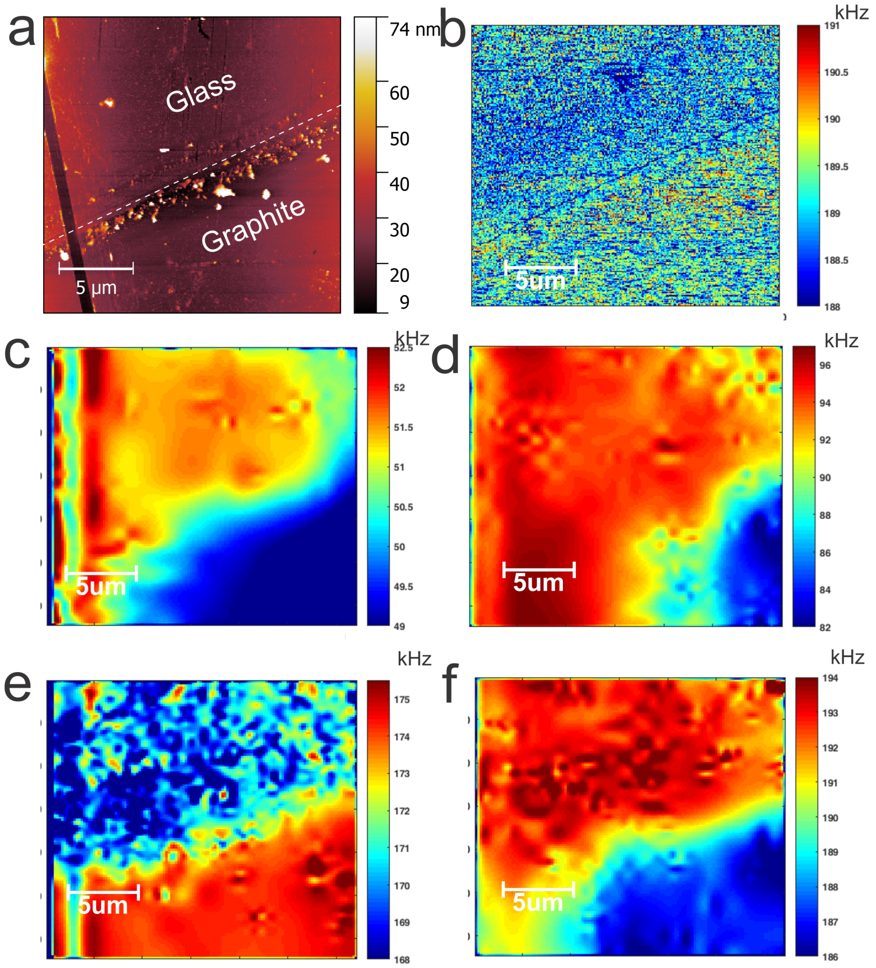

Figure 6: Results for graphite film over glass substrate. a) Conventional AFM topography, b) RT-AFAM for 188-191kHz window, and S-AFAM frequency map for: c) 49-53kHz window, d) 82-97kHz window, e) 168-176kHz window, and f) 186-194kHz window.

stiffness, which is product of effective contact and indentation modulus [8,9,18,37-45]. Using $k = 2aE^*$ and $E^* = (\frac{1}{M_{tip}} + \frac{1}{M_{sample}})^{-1}$, where $a \sim 11$nm was obtained using the methodology by [46], $M_{tip} = 170.33$GPa [36] and the proposed model, an indentation modulus mapping is obtained, see Figure 7. This mapping was computed using the results shown in Figure 6(c), (d), (e) and (f) and the database shown in Figure 5.

In Figure 7 (a) a higher difference between glass and graphite film can be seen when they are compared to RT-AFAM result. Even though the difference is very closed, S-AFAM can detect it a with higher resolution, see the histogram shown in Figure 7 (b). This difference is due to the glass substrate contribution and the thin thickness of the graphite film, where the indentation modulus are:

53.15MPa for glass substrate and 57.875MPa for the graphite film. These results agree with literature [47].

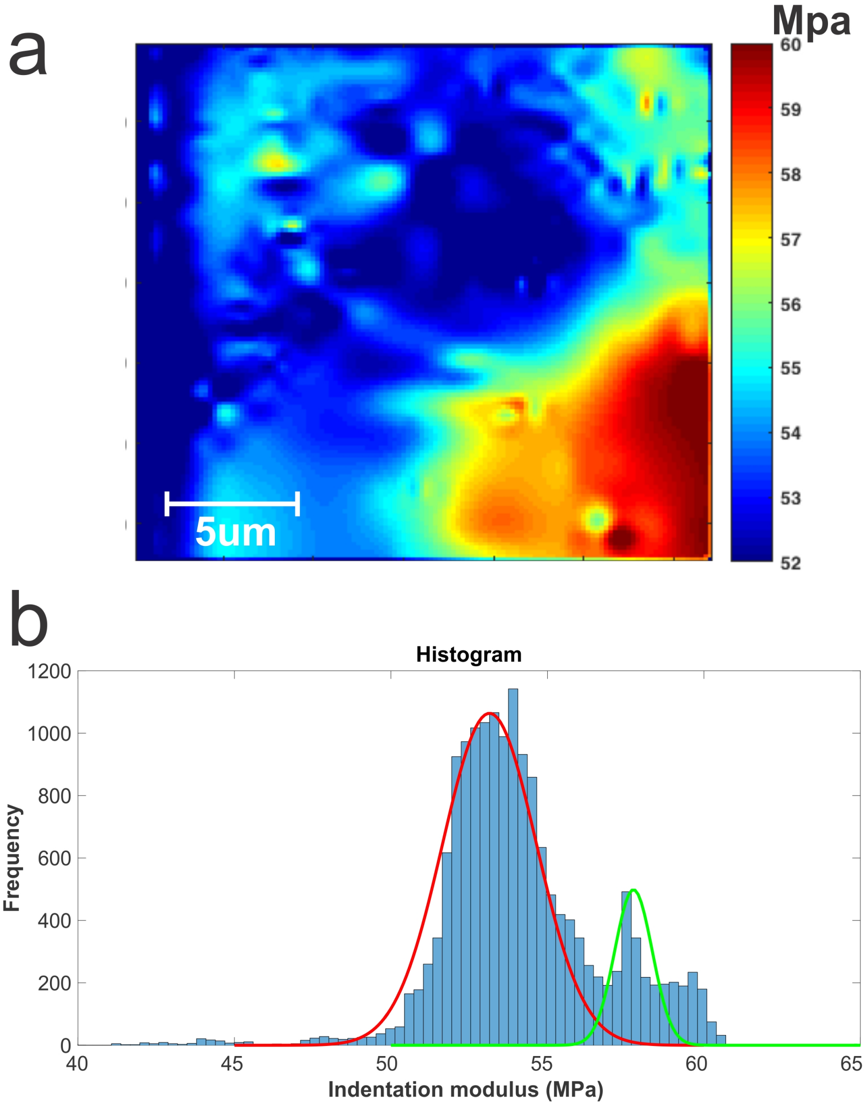

Figure 7: Results for graphite film over glass sample: a) Indentation modulus mapping and, b) histogram for the mapping.

The results make S-AFAM suitable for non-homogeneous material when the local mechanical properties over the material have closed resonance frequencies using white-noise. This way of excitation perturbs all the resonance frequencies at the same time, making the resonant modes extraction to be acquired in one measurement.

Even though the deflection signal from the photo-diodes is weak, when it is Fourier transformed, the amplitude increases significantly in the Fourier domain. This is possible due to the next Fourier transform property [25,31]

$$f(t) \leftrightarrow F(\omega), \tag{28}$$

for a real constant a,

$$f(at) \leftrightarrow \frac{1}{\mid a \mid} F\left(\frac{\omega}{a}\right), \tag{29}$$

when $\mid a \mid < 1$, it is possible to measure higher resonance frequencies without losing frequency resolution.

Theoretically, white-noise signal features an infinite flat-bandwidth which is impossible to generate [34,48]. Fortunately, this can be generated as an approximation using a waveform function generator, which makes white-noise an ideal signal for system identification because it can excite all the system dynamics instantaneously, i.e. it does not require time excitation such as sweep frequency[19]. Otherwise, it would not be possible to obtain using other kind of signals, i.e. *persistent excitation* [22]. Also, white-noise energy is lower than any other conventional signal avoiding either an electrical damage to the piezoelectric actuators or a physical damage to the sample. S-AFAM can be enhanced if a more capable instrumentation in real time is used, which allows an FFT to have a higher computational speed, and if a better white-noise signal generator is used, i.e. thermionic diode, which features a richer packet of frequencies.

Conclusions

S-AFAM can provide more information about aggregates, grain limits, mechanical stress of a grain, and so on when the local mechanical properties are closed, which makes these properties difficult to see when using a conventional technique. This achievement was possible because a white-noise excitation can extract more information about the tip-sample interaction than any other kind of signals using a power spectral density model and system theory. Additionally, S-AFAM does not have to look for a resonance frequency as other conventional techniques do, it only uses a reduced and optimal instrumentation without a lock-in amplifier so that the signal from the photo-diodes is not affected by the time constant of the lock-in amplifier. The resonant modes extraction is acquired in one single step of measurement, and the stored data is minimized in a hard-disk where the time taken for a measurement is important.

The results indicate that many contact resonance frequencies allow one indentation modulus value, where many values of indentation modulus would have been existed if other conventional technique would have been used. For this reason, it is important to have more than one vibrational mode of the tip-sample interaction since it provides quantitative knowledge about the contact stiffness, which is necessary in order to make further analysis about local mechanical properties.

S-AFAM provides images not only in high-resolution frequency, but also in depth resolution compared to conventional techniques, which loses resolution due to instrumentation and kind of signal excitation used for experimental purpose. Using S-AFAM, allows to carrying out depth analysis about local mechanical properties with a suitable model capable of making a relation between resonance frequency and indentation modulus.

Acknowledgements

The work was supported by the Projects LIDTRA LN-295261 and LIDTRA LN2015-254119 of CONACYT. The authors are grateful with the Laboratory for Research and Characterization of Minerals and Materials (LICAMM) of the University of Guanajuato.

References

1. Bhushan, B.; Fuchs, H. *Applied Scanning Probe Methods XI*; 2009.
2. Garcia, R.; Herruzo, E. *Nature* **2012**, *7*, 217–226.
3. Binnig, G.; Quate, C.; Gerber, C. *Physical Review Letters* **1986**, *56*, 930–933.
4. Rabe, U.; Amelio, S.; Kopycinska, M.; Hirsekorn, S.; Kempf, M.; Gȯken, M.; Arnold, W. *Surface and Interface Analysis* **2002**, *33*, 65–70.

5. Rabe, U.; Amelio, S.; Kester, E.; Scherer, V.; Hirsekorn, S.; Arnold, W. *Ultrasonics* **2009**, *38*, 430–437.

6. Enriquez, C.; Gervacio, J.; Cruz, E.; de Urquijo, P.; Gutierrez, B.; Espinoza, F. *Nanotechnology* **2012**, *23*, 495705.

7. Hahner, G. *Ultramicroscopy* **2010**, *110*, 801–806.

8. Mendels, D.; Lowe, M.; Cuenat, A.; Cain, M.; Vallejo, E.; Ellis, D.; Mendels, F. *Journal of Micromechanics and Microengineering* **2006**, *16*, 720.

9. Jesse, S.; Kalinin, S.; Proksch, R.; Baddorf, A.; Rodriguez, B. *Nanotechnology* **2007**, *18*, 435503.

10. Pharr, G.; Oliver, W.; Brotzen, F. *Journal of Materials Research* **1992**, *7*, 613–617.

11. Marinello, F.; Passeri, D.; Savio, E. *Acoustic Scanning Probe Microscopy*; 2013.

12. BD, H. *Annual Review of Materials Research* **2007**, *37*, 351–385.

13. Cuberes, M.; Assender, H.; Briggs, G.; Kolosov, O. *Journal of Physics D: Applied Physics* **2000**, *33*, 2347.

14. Garcia, R.; Proksch, R. *European Polymer Journal* **2013**, *49*, 1897–1906.

15. Rodriguez, B.; Callahan, C.; Kalinin, S.; Proksch, R. *Nanotechnology* **2007**, *18*, 475504.

16. Collins, L.; Belianinov, A.; Somnath, S.; Rodriguez, B.; Balke, N.; Kalinin, S.; Jesse, S. *Nanotechnology* **2016**, *27*, 105706.

17. Ebeling, D.; Babak, E.; S., S. *ACS nano* **2013**, *7*, 10387–10396.

18. Kos, A.; Hurley, D. *Measurement Science and Technology* **1964**, *19*, 015504.

19. Sader, J.; Borgani, R.; Gibson, C.; Haviland, B.; Higgins, M.; Kilpatrick, J.; Lu, J.; Mulvaney, P.; Shearer, C.; Slattery, A.; Thorén, P.; Tran, J.; Zhang, H.; Zhang, H.; Zheng, T. *Review of Scientific Instruments* **2016**, *87*, 093711.

20. Ogata, K. *Modern Control Engineering*; 2001.

21. Behar, A.; Iranzo, M. *Identificación y control adaptativo*; 2003.

22. Marino, R. *Nonlinear Control Design Design: Geometric, Adaptive and Robust*; 1995.

23. Marmarelis, V. *Applied Mathematical Modelling* **1980**, *4*, 117–124.

24. Speyer, J.; Chung, W. *Stochasic Processes, Estimation, and Control*; 2008.

25. Lathi, B. P. *Modern Digital and Analog Communication Systems*; 2009.

26. Sierra, F.; Vázquez, R.; Stark, R. *IEEE Transactions on nanotechnology* **2006**, *5*, 692–700.

27. Sierra, F.; Vázquez, R.; Stark, R. *Proceedings of the 2006 American Control Conference* **2006**, 532–537.

28. Sierra, F.; Vázquez, R.; Stark, R. *Transfer Function Analysis of Atomic Force Microscope Cantilevers* **2005**, *1*, .

29. Goodson, R. *Simulation by ASME* **1970**, *6*, 255–263.

30. Papoulis, A. *Probality, Random Variables, and Stochastic Processes*; 2007.

31. Proakis, J.; Manolakis, D. *Digital Signal Processing: Principles, Algorithms, and Applications*; 1996.

32. Chunming, Y.; Simon, D. *18th International Conference on ICSEng 2005* **2005**, 164–169.

33. R, E.; J, K. *Proceedings of the Sixth International Symposium on Micro Machine and Human Science* **1995**, 39–43.

34. Parsopoulos, K.; Vrahatis, M. *Particle Swarm Optimization and Intelligence: Advances and Applications*; 2010.

35. Ozcan, E.; Mohan, C. *Proceedings of the 1999 Congress on Evolutionary Computation, 1999* **1999**, *July*, 6–9.

36. Beltrán, F.; Muñoz, J.; Torres, J.; Torres, R.; Schneider, G. *Journal of Materials Research* **2012**, *21*, 3072–3079.

37. Gates, R.; Pratt, J. *Measurement Science and Technology* **2006**, *17*, 2852.

38. Ying, Z.; Reitsma, M.; Gates, R. *Review of Scientific Instruments* **2007**, *78*, 063708.

39. Langlois, E.; Shaw, G.; Kramar, J.; Pratt, J.; Hurley, D. *Review of Scientific Instruments* **2007**, *78*, 9.

40. Sader, J.; Chon, J.; Mulvaney, P. *Review of Scientific Instruments* **1999**, *70*, 3967–3969.

41. Green, C.; Lioe, H.; Cleveland, J.; Proksch, R.; Mulvaney, P.; Sader, J. *Review of Scientific Instruments* **2004**, *75*, 1988–1996.

42. Gibson, C.; Brandon, L.; Chris, A.; Rayment, T.; Sverre, M. *Ultramicroscopy* **2003**, *97*, 113–118.

43. Lozano, J.; Kiracofe, D.; Melcher, J.; Garcia, R.; Raman, A. *Nanotechnology* **2010**, *21*, 465502.

44. Gates, R.; Pratt, J. *Nanotechnology* **2012**, *23*, 375702.

45. Jesse, S.; Mirman, B.; Kalinin, S. *Applied Physics Letters* **2006**, *89*, 022906.

46. Yongda, Y.; Xue, B.; Hu, Z.; Zhao, X. *Ultramicroscopy* **2016**, *160*, 155–162.

47. Hurley, D.; Turner, J. *Journal of Applied Physics* **2004**, *95*, 2403–2407.

48. Wiener, N. *The Extrapolation, Interpolation and Smoothing of Stationary Time Series with Engineering Applications*; 1964.